Low Temperature Physics/Fizika Nizkikh Temperatur, 2018, v. 44, No. 4, pp. 449–454

Crystalline phase detection in glass ceramics by EPR spectroscopy

A. Antuzevics, U. Rogulis, A. Fedotovs, and A.I. Popov

Institute of Solid State Physics, University of Latvia, 8 Kengaraga, LV-1069 Riga, Latvia
E-mail: andris.antuzevics@gmail.com

Received September 17, 2017, published online February 26, 2018

The advances of EPR spectroscopy for the detection of activators as well as determining their local structure in the crystalline phase of glass ceramics is considered. The feasibility of *d*-element (Mn^{2+}, Cu^{2+}) and *f*-element (Gd^{3+}, Eu^{2+}) ion probes for the investigation of glass ceramics is discussed. In the case of Mn^{2+}, the information is obtained from the EPR spectrum superhyperfine structure, for Gd^{3+} and Eu^{2+} probes – from the EPR spectrum fine structure, whereas for Cu^{2+} ions the changes in the EPR spectrum shape could be useful. The examples of EPR spectra of the above-mentioned probes in oxyfluoride glass ceramics are illustrated.

PACS: 76.30.–v Electron paramagnetic resonance and relaxation;
61.72.Hh Indirect evidence of dislocations and other defects.

Keywords: electron paramagnetic resonance, paramagnetic ions, glass ceramics.

1. Introduction

An actual problem for the development of glass ceramics is ensuring that the majority of dopant ions embed the crystalline phase of the material. Crystalline phases in glass ceramics are usually detected by x-ray diffraction (XRD) measurements and visualized by transmission electron microscopy (TEM) photographs, however, these methods do not provide the essential information about the activator local structure. Absorption and luminescence spectra, on the other hand, can indicate changes in the local environment around the luminescence centres, however, structure sensitive magnetic resonance spectroscopy techniques should be employed to reveal the detailed nature of defects in glass ceramics. Electron paramagnetic resonance (EPR) is one of the most convenient and informative methods for the study of point defects in crystals and glasses [1–11], however, there has been only a limited number of applications to glass ceramics [12–21].

A choice of optimal temperature is necessary to ensure the best EPR signal intensity and avoid temperature caused line broadening in the spectra. For this reason EPR measurements are usually done at cryogenic temperatures, e.g. at liquid nitrogen boiling point (77 K).

The present paper provides a review of EPR results of paramagnetic probes studied in glass ceramics as well as our recent data on Mn^{2+}, Cu^{2+} and Gd^{3+} ions in oxyfluoride glass ceramics.

2. Experimental

Glasses were prepared by the conventional melt quenching technique. Batches of 8 g (see Table 1) were mixed and melted at (1450 ± 10) °C in covered alumina crucibles and quenched by pouring the melts onto a stainless steel plate. The glass ceramics were obtained by an isothermal heat treatment of the transparent precursor glass (PG) at the indicated temperature. The sample abbreviation includes the paramagnetic probe (Mn, Cu or Gd) as well as the crystalline phase of the glass ceramic samples (C — CaF_2, S — SrF_2, B — BaF_2, N — $NaLaF_4$). The last number in the sample abbreviation is the heating temperature in °C. For example, Mn_C_700 is the glass ceramic obtained after heating the Mn_C_PG (precursor glass) composition sample at 700 °C for 1 h.

X-ray diffraction (XRD) measurements with PANalytical X'Pert Pro diffractometer were made to identify the crystalline phases present in glass ceramics.

Table 1. Compositions used for glass preparation

Abbreviation	Composition
Mn_C	$46SiO_2$–$20Al_2O_3$–$8CaCO_3$–$25CaF_2$–$0.1MnO$
Cu_C	$46SiO_2$–$20Al_2O_3$–$8CaCO_3$–$25CaF_2$–$0.1CuO$
Gd_N	$63SiO_2$–$7Al_2O_3$–$16Na_2CO_3$–$9NaF$–$5LaF_3$–$0.1GdF_3$
Gd_S_01	$40SiO_2$–$25Al_2O_3$–$15Na_2CO_3$–$1EuF_3$–$19SrF_2$–$0.1GdF_3$
Gd_S_10	$40SiO_2$–$25Al_2O_3$–$15Na_2CO_3$–$1EuF_3$–$18SrF_2$–$1.0GdF_3$
Gd_S_40	$40SiO_2$–$25Al_2O_3$–$15Na_2CO_3$–$1EuF_3$–$15SrF_2$–$4.0GdF_3$

EPR spectra were measured at 77 K with a conventional X-band spectrometer (≈ 9.1 GHz). The magnetic field was callibrated using a polycrystalline DPPH reference — an organic chemical compound which is commonly used in EPR spectroscopy.

The structural models were visualised using VESTA software [22,23].

3. Results and discussion

3.1. Mn^{2+}

Manganese is one of the most commonly used paramagnetic probes for local structure investigations via EPR spectroscopy. The characteristic Mn^{2+} EPR spectrum arises from the hyperfine structure (HFS) interaction between the d^5 shell electron cloud effective spin $S = 5/2$ and 100% abundant ^{55}Mn isotope nuclear spin $I = 5/2$. The resonance positions in single crystals are also strongly dependent on the Mn^{2+} centre symmetry determined by the surrounding ligand field. Thus, the effective spin-Hamiltonian (SH) is:

$$H = \beta gBS + \sum_k \sum_q f_k b_k^q O_k^q + ASI \qquad (1)$$

where β is the Bohr magneton; g — the g-factor; B — the applied magnetic field; f_k — numerical constants; b_k^q — zero field splitting (ZFS) parameters depending on the site symmetry; O_k^q — spin operators and A — the hyperfine interaction constant.

In vitreous media Mn^{2+} EPR spectrum consists of a signature sextet (see Fig. 1) centred at $g = 2.0$ caused by the hyperfine interaction, whereas the angularly dependent ZFS part usually is not resolved. The magnetic field range of the spectrum is characterized by the magnitude of isotropic hyperfine interaction constant A, and is an indicator of local chemical environment around the impurity. A more ionic bonding to the surrounding ligands results in a larger A value [24].

In InF_3 based glass ceramics, heat treatment of the precursor glass has caused the increase of the signal/noise ratio of the characteristic sextet indicating localization of a larger part of Mn^{2+} ions in highly order sites [12]. In tellurite borate glass ceramics, local Mn^{2+} site symmetry has been monitored from SH parameters as a function of manganese content in the composition [13]. Oxyfluoride

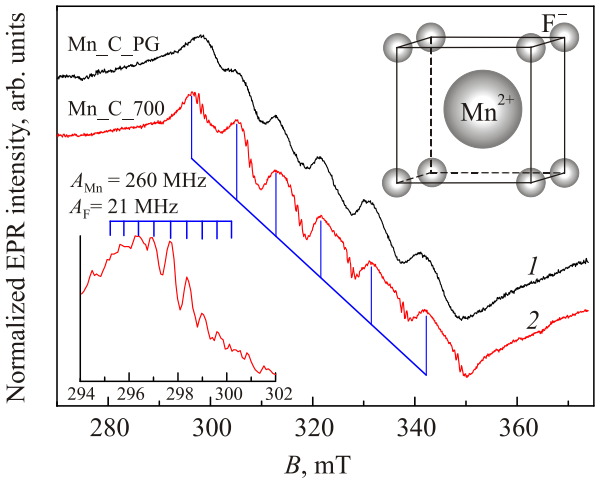

Fig. 1. (Color online) EPR spectra of the manganese doped glass (*1*, black) and the glass ceramic (*2*, red) containing CaF_2. Inset shows the eightfold coordinated Mn^{2+} site in CaF_2 nanocrystals.

glass ceramics containing fluorite structure crystallites (CaF_2, SrF_2, BaF_2) have shown particularly interesting results — additional superhyperfine structure (SHFS) splitting of each spectral line after the precipitation of fluoride nanocrystals in the glass matrix can be observed [14–17].

Figure 1 shows Mn_C composition glass and the respective glass ceramic obtained after the heat treatment at (700 ± 10) °C. The superimposed SHFS in the glass ceramic is caused by the interaction between the Mn^{2+} effective spin S and the spins of N nearest fluorine nuclei $I_F = 1/2$. As a result, each HFS line is split into $2NI_F + 1$ components with binomial intensity distribution. Splitting into 9 components in our case means that Mn^{2+} ions substitute Ca^{2+} ions in CaF_2 nanocrystals and are surrounded by 8 equidistant fluorine nuclei. The results obtained here are consistent with Refs. 14–17.

EPR studies of manganese paramagnetic probes in glass ceramics thus yields information not only about the formation of crystallites in the glass matrix, but also helps to assess the first coordination sphere around the dopant ions in the crystalline phase.

3.2. Cu^{2+}

Copper ions are commonly used spin probes for local structure investigations in vitreous media [25–29]. For the interpretation of characteristic Cu^{2+} spectrum (see Fig. 2), an axial SH should be applied:

$$H = \beta g_{\parallel} B_z S_z + \beta g_{\perp} \left(B_x S_x + B_y S_y \right) + \\ + A_{\parallel} S_z I_z + A_{\perp} \left(S_x I_x + S_y I_y \right). \qquad (2)$$

The Cu^{2+} ion has $S = 1/2$ and $I = 3/2$ for both isotopes ^{63}Cu and ^{65}Cu and thus a HFS splitting into four resonances is expected for both parralel and perpendicular compo-

nents of the g tensor. Such spectral features are characteristic of Cu^{2+} ions in distorted octahedral sites elongated along the z-axis. The SH parameter values indicate the strength of the surrounding ligand field.

Literature about the incorporation of copper ions in the crystalline phase of glass ceramics, on the other hand, is somewhat scarce. Previous study of Cu^{2+}-doped InF_3 based glass ceramics has observed a relatively broad Gaussian line superimposing the glassy spectrum after the heat treatment of the precursor glass, however, its origin was related to oxygen/water content in the atmosphere during the glass preparation [12]. Here Fig. 2 shows the EPR spectra of Cu_C composition glass and the corresponding glass ceramic heated at (700 ± 10) °C. Spectrum shape near $g = 2.0$ has changed, however, the lack of structure in this resonance prohibits additional information about the nature of this paramagnetic centre. Nevertheless, changes in the EPR spectra shape observed after the creation of crystallites in the glass allows, in principle, to detect the crystalline phase in glass ceramics.

3.3. Gd^{3+}

Most potential applications of glass ceramics revolve around the luminescence of rare earth ions, therefore, the local structure of trivalent defects in these systems is of great interest. Unfortunately, direct observation of most rare earths is problematic either due to the lack of paramagnetic ground state or by the necessity of liquid helium temperatures to observe the spectrum. The unusually long spin-lattice relaxation time of gadolinium makes it one of the most useful paramagnetic probes for studying the "glass → glass ceramic" transition even at room temperature. The ground state of Gd^{3+} is an S-state ($4f^7$; $S = 7/2$) and the splitting in external magnetic field is described by:

$$H = \beta gBS + \sum_k \sum_q f_k b_k^q O_k^q \,. \qquad (3)$$

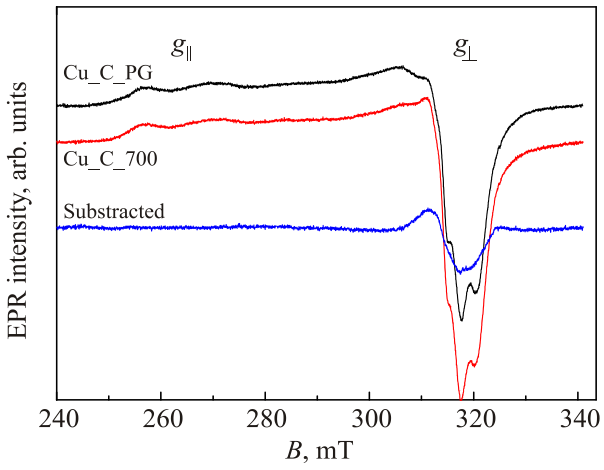

Fig. 2. (Color online) EPR spectra of the copper doped glass and glass ceramic containing CaF_2.

Gd^{3+} in disordered media is characterized by the signature U-type (ubiquitous) spectrum with resonances at $g_{\text{eff}} = 6.0$, 2.8 and 2.0. Coordination with a relatively large number of ligands at inequivalent distances can be simulated by taking a relatively broad distribution in second-order ZFS parameters [30,31]. In crystalline media, the nature of Gd^{3+} local environment is host sensitive and can yield valuable information about the material in study [32].

After precipitation of a crystalline phase in the glass matrix, intensive resonances centred at $g = 2.0$ usually superimpose the U-type spectrum [12,18]. An example is shown in Figs. 3 and 4 — Gd_N composition glass and the corresponding glass ceramic containing $NaLaF_4$ nanocrystals. The XRD spectra clearly show the formation of $NaLaF_4$ nanocrystals in the glass matrix. Meanwhile, the intense new EPR signal indicates efficient incorporation of trivalent rare earth impurities in the crystalline phase of glass ceramics. For a better understanding of gadolinium centres in $NaLaF_4$, EPR angular variations in single crystalline sample should be studied.

In order to extract the most from EPR spectra, an optimal concentration of paramagnetic impurities should be used. In Fig. 5 glass ceramics containing SrF_2 crystalline phase and Gd^{3+} ions in different concentrations are compared. The fine structure is best resolved at relatively lower dopant concentration and is significantly broadened due to the dipolar interaction between the paramagnetic centres at higher doping levels. At high concentration, various forms of composite defects such as gadolinium ion pairs and clusters may also be present.

Gd^{3+} in oxyfluoride glass ceramics containing fluorite structure crystalline phase have been studied recently [19,20]. Main results for compositions containing CaF_2, SrF_2 and BaF_2 are summarized in Fig. 6. EPR spectrum structure strongly depends on the local symmetry around Gd^{3+} impurities in these nanocrystals. When trivalent gadolinium

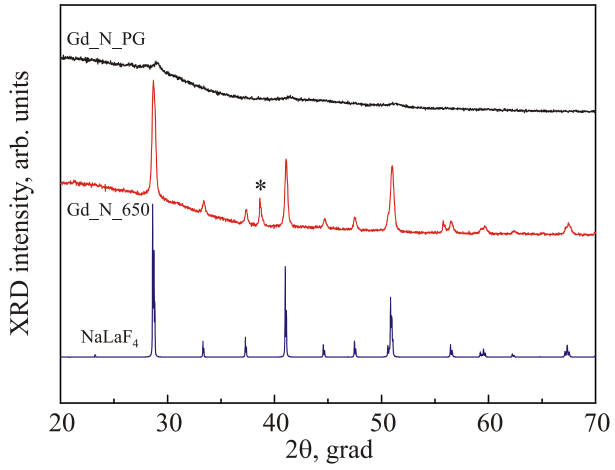

Fig. 3. (Color online) XRD spectra of the gadolinium doped glass and glass ceramic containing $NaLaF_4$. The blue curve is the calculated polycrystalline $NaLaF_4$ diffractogram. Peak marked with * belongs to the NaF crystalline phase.

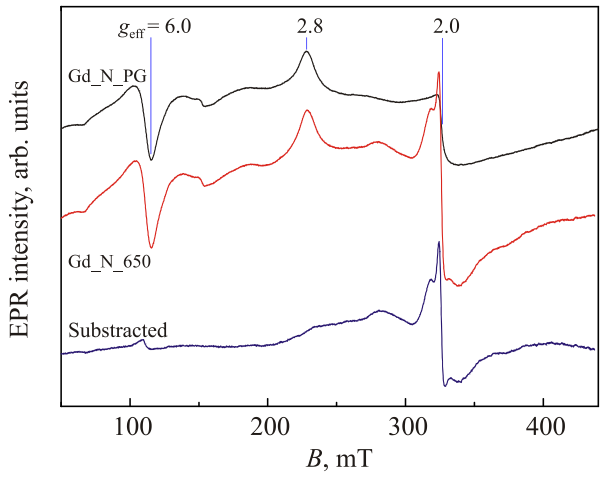

Fig. 4. (Color online) EPR spectra of the gadolinium doped glass and glass ceramic containing $NaLaF_4$.

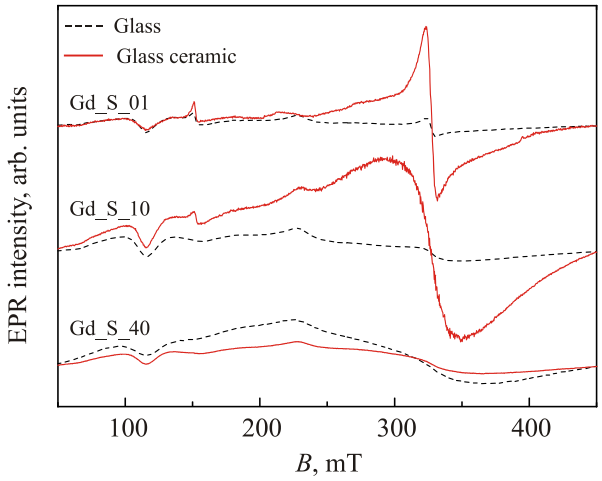

Fig. 5. (Color online) Gd^{3+} concentration dependance of the EPR spectra of glasses and glass ceramics containing SrF_2.

replaces the divalent cation, a charge compensation is necessary. Depending on the compensator orientation in the lattice, various forms of Gd^{3+} centres are possible in fluorite structure crystals — cubic centres when the compensator is located far from the impurity [33], tetragonal centres where usually an interstitial fluorine anion located along [100] direction distorts the original cubic configuration [34] and trigonal centres if the charge is compensated by an additional impurity along the [111] direction [35]. The mentioned Gd^{3+} symmetries in fluorite type crystals are illustrated in Fig. 7. When Gd^{3+} replaces the similarly sized Ca^{2+} ions in glass ceramics containing CaF_2, the EPR spectrum is dominated by Gd^{3+} in local cubic symmetry crystal field [19], whereas substitution of significantly larger Ba^{2+} ions in glass ceramics containing BaF_2 leads to an EPR signal characterized by SH parameters for trigonal site symmetry [20].

To summarize, EPR spectral features of Gd^{3+} ions are sensitive to the local environment and are effective for detecting the presence of crystalline phase in glass ceramics.

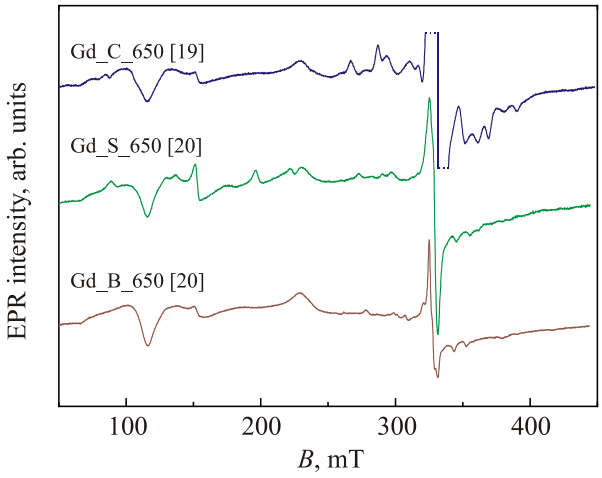

Fig. 6. (Color online) EPR spectra of glass ceramics containg CaF_2 [19], SrF_2 and BaF_2 [20] nanocrystals.

The results obtained from the studies of Gd^{3+} EPR spectra could also be used to analyse non-magnetic trivalent rare earth ions, local structure of which cannot be studied by magnetic resonance spectroscopy.

3.4. Eu^{2+}

The electron configuration of Eu^{2+} ground state is the same as for Gd^{3+} ($4f^7$; $S = 7/2$), however, the EPR spectrum is complicated by the HFS interaction with europium isotopes ^{151}Eu and ^{153}Eu ($I = 5/2$). As a result, each ZFS component is further split into two sets of sextets and SH (1) must be used for interpretation. In glass ceramics doped with Eu^{2+}, the randomly orientated crystallites are, therefore, expected to generate much broader lines than similar systems with Gd^{3+}. EPR studies of europium doped systems may also be hindered by the presence of stable non-magnetic Eu^{3+} ions which are generally more abundant unless special reduction has been carried out during the sample preparation.

Eu^{2+} EPR signal has been observed in glass ceramics containing $BaBr_2$. Successful simulation of the spectrum with the single crystal SH data confirmed that the signal originates from the $BaBr_2$ crystalline phase of glass ceramics [21].

Europium doped glass ceramics are promising materials for optical applications and the luminescence properties have been studied extensively in various systems containing fluorite type nanocrystals [36–38]. As well-known from the literature, the broad emission of Eu^{2+} $5d \rightarrow 4f$ luminescence is sensitive to the local ligand field and, thus, some EPR data could contribute to a better understanding of these systems.

A recent study [39], in particular, focuses on monitoring the valence state of europium ions in different composition glass ceramics containing SrF_2. Sharp lines in the EPR spectra can be observed after the heat treatment of the precursor glass at high temperatures, where $Eu^{3+} \rightarrow Eu^{2+}$ reduction and incorporation into crystalline phases is efficient,

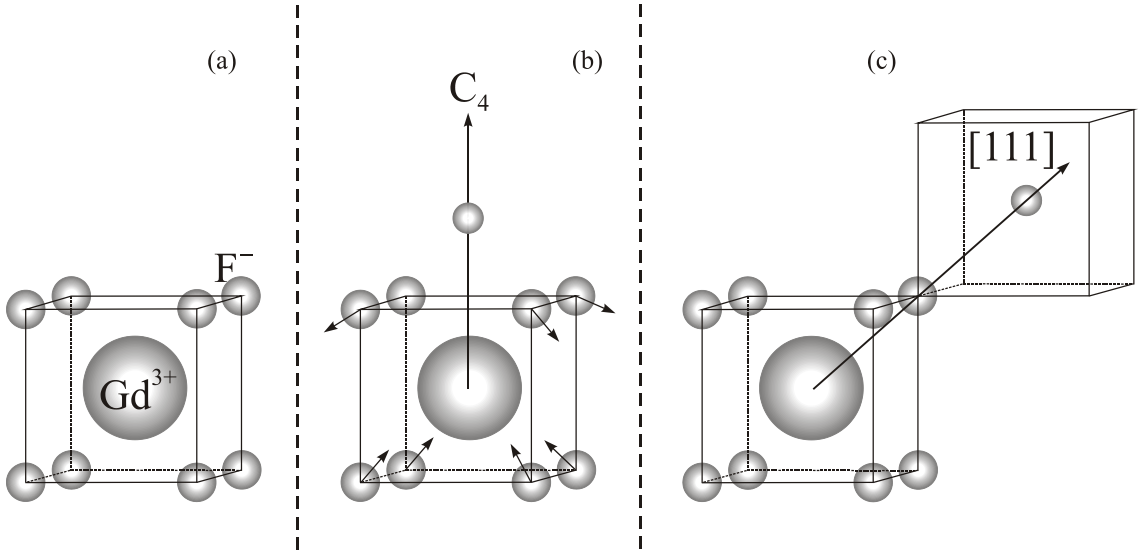

Fig. 7. Possible Gd^{3+} centres in fluorite structure single crystals: cubic (a), tetragonal (b), trigonal (c) centers. Adapted from [33], [34] and [35] respectively.

whereas Eu^{2+} ions in the glassy matrix can be detected by the signature *U*-type spectrum. Combining the EPR data with photoluminescence spectra allows a direct attribution of Eu^{2+} local structure to particular optical properties.

4. Conclusions

1. *d*-element (Mn^{2+}, Cu^{2+}) and *f*-element (Gd^{3+}, Eu^{2+}) paramagnetic probes are suitable for detecting the incorporation of activators in the crystalline phase of glass ceramics.

2. Variation of Mn^{2+} and Cu^{2+} spectral shapes after the precipitation of crystalline phases in the glass matrix indicates the change of local environment around the impurities. Coordination of Mn^{2+} in nanocrystals can be determined if the SHFS is resolved in the EPR spectrum.

3. Intensive EPR signal emerges and overlays the glassy *U*-type spectrum after the heat treatment of the precursor glass if Gd^{3+} ions embed in the crystalline phase. The resonance positions depend strongly on the local crystalline field, therefore, local site symmetry around the impurity can be determined.

4. Europium ion valence state can be monitored from EPR spectra measurements. Similarly to Gd^{3+}, Eu^{2+} ions in the glass matrix exhibit the signature *U*-type spectrum and incorporation into crystalline phases of glass-ceramics can be determined via additional EPR spectrum fine structure.

Acknowledgements

The authors thank Meldra Kemere and Dr. Edgars Elsts for sample synthesis and Reinis Ignatans for XRD measurements. Financial support of Latvian-Ukrainian Joint Research Project No. LV-UA/2016/1 is acknowledged.

1. J. Kliava and J. Purans, *J. Magn. Res.* **40**, 33 (1980).
2. U. Rogulis, C. Dietze, T. Pawlik, T. Hangleiter, and J.M. Spaeth, *J. Appl. Phys.* **80**, 2430 (1980).
3. A. Antuzevics, U. Rogulis, A. Fedotovs, D. Berzins, V.N. Voronov, and J. Purans, *Phys. Scr.* **90** (2015).
4. T. Kärner, S. Dolgov, A. Lushchik, N. Mironova-Ulmane, S. Nakonechnyi, and E. Vasil'chenko, *Radiat. Eff. Defs. Solids* **155**, 171 (2001).
5. Y.V. Kolk and A.C. Lushchik, *Sov. Phys. Solid State* **28**, 805 (1986) [*Fiz. Tverd. Tela* **28**, 1432 (1986)].
6. A.Ch. Lushchik and A.G. Frorip, *Phys. Status Solidi B* **161**, 525 (1990).
7. S. Dolgov, T. Kärner, A. Lushchik, A. Maaroos, N. Mironova-Ulmane, and S. Nakonechnyi, *Radiat. Prot. Dosim.* **100**, 127 (2002).
8. N. Mironova-Ulmane, V. Skvortsova, A. Pavlenko, E. Feldbach, A. Lushchik, Ch. Lushchik, V. Churmanov, D. Ivanov, V. Ivanov, and E. Aleksanyan, *Radiat. Meas.* **90**, 122 (2016).
9. I. Romet, M. Buryi, G. Corradi, E. Feldbach, V. Laguta, E. Tichy-Rács, and V. Nagirnyi, *Opt. Mater.* **70**, 184 (2017).
10. V. Seeman, S. Dolgov, and A. Maaroos, *Physica B* **513**, 69 (2017).
11. S.A. Dolgov, T. Kärner, A. Lushchik, A. Maaroos, S. Nakonechnyi, and E. Shablonin, *Phys. Solid State* **53**, 1244 (2011) [*Fiz. Tverd. Tela* **53**, 1179 (2011)].
12. R.W.A. Franco, J.F. Lima, C.J. Magon, J.P. Donoso, and Y. Messaddeq, *J. Non-Cryst. Solids* **352**, 3414 (2006).
13. T. Satyanarayana, M.A. Valente, G. Nagarjuna, and N. Veeraiah, *J. Phys. Chem. Solids* **74**, 229 (2013).
14. A. Fedotovs, D. Berzins, O. Kiselova, and A. Sarakovskis, *IOP Conf. Ser. Mater. Sci. Eng.* **38**, 12047 (2012).

15. A. Fedotovs, D. Berzins, O. Kiselova, A. Sarakovskis, and U. Rogulis, *IOP Conf. Ser. Mater. Sci. Eng.* **23**, 12018 (2011).
16. D. Berzins, A. Fedotovs, O. Kiselova, and A. Sarakovskis, *IOP Conf. Ser. Mater. Sci. Eng.* **38**, 12046 (2012).
17. A. Fedotovs, D. Berzins, A. Sarakovskis, U. Rogulis, and G. Doke, *IOP Conf. Ser. Mater. Sci. Eng.* **15**, 12068 (2010).
18. M. Mohapatra, B. Rajeswari, N.S. Hon, R.M. Kadam, M.S. Keskar, and V. Natarajan, *Ceram. Int.* **41**, 8761 (2015).
19. A. Fedotovs, A. Antuzevics, U. Rogulis, M. Kemere, and R. Ignatans, *J. Non-Cryst. Solids* **429**, 118 (2015).
20. A. Antuzevics, M. Kemere, and R. Ignatans, *J. Non-Cryst. Solids* **449**, 29 (2016).
21. S. Schweizer, G. Corradi, A. Edgar, and J.-M. Spaeth, *J. Phys. Condens. Matter* **13**, 2331 (2001).
22. K. Momma and F. Izumi, *J. Appl. Crystallogr.* **41**, 653 (2008).
23. K. Momma and F. Izumi, *J. Appl. Crystallogr.* **44**, 1272 (2011).
24. F.J. Owens, *J. Chem. Phys.* **57**, 118 (1972).
25. G.N. Devde, G. Upender, V. Chandra Mouli, and L.S. Ravangave, *J. Non-Cryst. Solids* **432**, 319 (2016).
26. S. Prakash Singh, R.P.S. Chakradhar, J.L. Rao, and B. Karmakar, *J. Magn. Magn. Mater.* **346**, 21 (2013).
27. A. Hameed, G. Ramadevudu, M. Shareefuddin, and M.N. Chary, *AIP Conf. Proc.* **1591**, 842 (2014).
28. A. Bhogi and P. Kistaiah, *Phys. Chem. Glas. Eur. J. Glas. Sci. Technol. Part B* **56**, 197 (2015).
29. B. Sreedhar, C. Sumalatha, and K. Kojima, *J. Non-Cryst. Solids* **192–193**, 203 (1995).
30. C.M. Brodbeck and L.E. Iton, *J. Chem. Phys.* **83**, 4285 (1985).
31. C. Legein, J.Y. Buzaré, G. Silly, and C. Jacoboni, *J. Phys. Condens. Matter* **8**, 4339 (1996).
32. H.A. Buckmaster and Y.H. Shing, *Phys. Status Solidi* **12**, 325 (1972).
33. J. Sierro, *Phys. Lett.* **4**, 178 (1963).
34. W.-Q. Yang, Y. Zhang, Y. Lin, and W.-C. Zheng, *J. Magn. Reson.* **227**, 62 (2013).
35. C. Yang, S. Lee, and A.J. Bevolo, *Phys. Rev. B* **13**, 2762 (1976).
36. Q. Luo, X. Qiao, X. Fan, S. Liu, H. Yang, and X. Zhang, *J. Non-Cryst. Solids* **354**, 4691 (2008).
37. Q. Luo, X. Qiao, X. Fan, and X. Zhang, *J. Am. Ceram. Soc.* **93**, 2684 (2010).
38. K. Biswas, A.D. Sontakke, R. Sen, and K. Annapurna, *J. Fluoresc.* **22**, 745 (2012).
39. A. Antuzevics, M. Kemere, G. Krieke, and R. Ignatans, *Opt. Mater.* **72**, 749 (2017).